crystals

Article

Microstructure Evolution of AZ91 Magnesium Alloy Welded Joint under Magnetic Field and $NiCl_2$ Activated Flux

Guiqing Zhang *, Yinglei Ren and Yunhai Su

School of Materials Science and Engineering, Shenyang University of Technology, Shenyang110870, China
* Correspondence: guiqingzhang@sut.edu.cn; Tel.: +139-9814-5109

Abstract: As the lightest engineering materials, magnesium alloys have been widely used. Because of the specific chemical and physical characteristics, the weldability of magnesium alloy is poor. Adopting suitable welding technology and improving the quality of magnesium alloy welded joints is key to their successful application. According to previous research data, it was found that the combined action of magnetic field and activated flux has a positive effect on improving-welding efficiency and improving the properties of a welded joint, butanalysis of microstructure evolution is insufficient. In this paper, AZ91 magnesium alloy was welded by TIG welding with activated flux and external longitudinal AC magnetic field. The phase composition and microstructure evolution were investigated. The experimental results revealed that the phase composition of welded joint was not changed due to the introduction of the magnetic field and activated flux, the growth patterns of grain in the weld seam and heat-affected zone were different. When the activated flux amount was 3 mg/cm^2 with the effect of the magnetic field, the grain size of the weld seam was the finest, which was 18.96 µm. However, the grain size of the weld seam was larger than that of base metal. The crystallographic characteristics of grain boundaries in the weld seam and base metal were both LAGBs. The microstructure of the weld seam was messier than the base metal due to the larger misorientation angle. Under the combined action of the magnetic field and activated flux, the crystallization nucleation condition of the molten pool was changed, the formation of twins was promoted, and the crystal could selectively grow parallel with the (0001) basal plane.

Keywords: EBSD; magnesium alloy; microstructure evolution; activated flux; magnetic field

check for updates

Citation: Zhang, G.; Ren, Y.; Su, Y. Microstructure Evolution of AZ91 Magnesium Alloy Welded Joint under Magnetic Field and $NiCl_2$ Activated Flux. *Crystals* **2022**, *12*, 1389. https://doi.org/10.3390/cryst12101389

Academic Editors: Ireneusz Zagórski, Mirosław Szala and Pavel Lukáč

Received: 28 August 2022
Accepted: 24 September 2022
Published: 29 September 2022

1. Introduction

With the rapid development of modern industry, the application of magnesium and magnesium alloys has rapidly increased at a rate of more than 20% per year. They have become one of the most important basic materials for the development of the national economy because magnesium alloy, as the lightest of all structural materials, has properties including high specific strength, good damping capacity, excellent machinability, and ease of recycling. It is these properties that find magnesium alloys widely applied in aerospace, transportation, biomedicine and 3C products [1–4]. As a structural material, the connection of magnesium alloys should be considered in practical engineering applications. Welding is the most commonly used method of connection. However, the characteristics of magnesium alloy, including active chemical properties, low melting point, high coefficient of thermal conductivity, high thermal conductivity, and electrical conductivity, determined its poor welding performance. Therefore, the development and application of welding technology holds important practical significance for the industrialization of magnesium alloy. Extensive research concerning welding technologies has been carried out in recent years. Lu et al. [5] studied the welding properties of EW75 magnesium alloy welded by TIG. They found that grain size was affected by the welding current. Electron beam welding (EBW) for magnesium alloy was researched by Yang et al. [6] and Asahina T et al. [7]. Zhang et al. [8] reported the relationships between the processing parameters and the welding modes, dimensions, microstructures, and defects for pulsed laser spot welding of AZ31 alloy. The results showed that the weld diameter and penetration were not affected by processing parameters and the microstructure cracks occurred in keyhole mode. Shahnam et al. [8,9] observed that ultra-fine-grained structure could be obtained in AZ31 magnesium alloy welded joint under submerged friction stir processing (SFSP) compared to friction stir processing (FSP). Mironov et al. [10] studied the influence of welding temperature on material flow during FSW of AZ31 magnesium alloy. When the temperature was above 0.8 Tm, the transitional component of material flow disappeared. Among the welding technologies mentioned above, TIG welding has become a commonly used technology due to its adaptability, stability, and economy [11].

The primary limitation of TIG welding is low productivity due to its low deposition and shallow penetration [12,13]. Thus, thicker plates require a higher number of passes for welding. To overcome this limitation, an activated tungsten insert gas (A-TIG) welding process has been developed. In this process, the activated flux is used on the plate surface before welding, an increase by three times in the penetration could be achieved as compared to conventional TIG welding [14,15]. Hence, A-TIG welding could improve production efficiency and reduce production costs. Many researches regarding A-TIG welding of magnesium alloy have been published [16–21]. These researches proposed the specific activated fluxes increased the penetration and the mechanism for the high penetration, but the finer grain size was hardly found in the welded joint.

Grain refinement can improve the mechanical properties of welded joints. Aiming to achieve grain refinement of magnesium alloy A-TIG welded joints, several methods have been developed, such as selecting the appropriate welding parameters [22–24], post-weld heat treatment [24,25], and nanoparticles strengthening A-TIG [26]. However, there are limitations associated with the above methods. For instance, no obvious grain refinement was observed in the weld seam using the first method, the treatment process was a little complex using the second method, and the weld penetration was decreased using the last method. The present investigation aimed to refine the grains of magnesium alloy A-TIG welded joint as well as maintain high weld penetration. Thus, the external magnetic field was considered to apply during the A-TIG welding process. Applying an external magnetic field was not only a simple process, but also low in energy consumption [27]. Moreover, the external magnetic field could change the nucleation conditions of liquid metal through non-contact electromagnetic influence, refine the grains to improve the performance of the metal, and had no pollution in the liquid metal [28–30]. The longitudinal magnetic field could obtain higher penetration compared to other magnetic fields because the charged particles in the arc moved downward in a spiral under the effect of the Lorentz force. According to previous studies [31–33], we found that a longitudinal alternating magnetic field could refine the crystal grain and improve the tensile strength and hardness of magnesium alloy at proper parameters. Hence, in this paper, a longitudinal alternating magnetic field was applied in the A-TIG welding process. The effect of the magnetic field and activated flux on increasing the penetration and improving mechanical properties of welded joints was confirmed in our prior work [34]. However, the study of microstructure evolution and grain growth is not sufficient. Therefore, further study and detailed discussion are explained in this paper.

2. Materials and Methods

The base metals used in the present study were commercial AZ91 magnesium alloy (Baienwei, China) plates with the dimension of 100 mm × 100 mm × 5 mm. We polished the smooth surface with abrasive paper to remove oxide film and impurities and dried it after cleaning. Using anhydrous ethanol to prepare aluminum powder into a paste, it was evenly applied to the surface of the substrate, with a thickness of 0.5 mm. The chemical composition is given in Table 1.

Table 1. Chemical composition of the base metal (wt%).

Al	Zn	Mn	Si	Cu	Fe	Mg
8.3–9.7	0.35–1	0.15–0.5	<0.01	<0.03	<0.005	Balance

Before this experiment, the $NiCl_2$ flux was supplied in powder form and mixed with ethanol to produce a fine paste. A brush was used to apply the flux paste over the area to be welded. The amounts of the $NiCl_2$ coating on different specimens were 1 mg/cm^2, 2 mg/cm^2, 3 mg/cm^2, 4 mg/cm^2, 5 mg/cm^2, respectively. The specimens with coatings were placed for 24 h at room temperature, then welded using a WSE-50 welding machine. A magnetic coil installed directly on the welding torch was used as the source of a longitudinal magnetic field. The parameters of welding current, excitation current, and oscillation frequency of the magnetic field were the optimal parameters obtained through orthogonality optimization experiments, which were 85 A, 3.5 A, 30 Hz, respectively. Welding speed of was held at 300 mm/min. The extension of tungsten of 2 mm was maintained. The shielding gas used for the arc torch was pure argon, the flowing rate of which was 10–15 L/min.

After welding, the specimens were cut across the seam from the welded plates and then were prepared using standard metallographic procedures. The metallographic specimens were etched in a solution with 20 mL ethylene glycol, 60 mL glacial acetic acid, 1 mL nitric acid, and 19 mL distilled water, and then observed by scanning electron microscopy (Hitachi S-3400, Tokyo, Japan). The phase composition in the welded joints was determined by XRD. X-ray diffraction (XRD) patterns were obtained with a diffractometer, model MAXima-7000. The parameters were as follows: Cu Ka radiation with a graphite monochromator, 40 kV, and 100 mA. The XRD measurements were performed in a range of 20–80° (2θ) using a 0.02° step size with 30 s time per step. The microstructure morphology of welded joints was studied by OM, SEM, and TEM. EBSD (QUANTAX Berlin, Germany) texture analysis was conducted on a field emission scanning electron microscope of ZEISS G300. (Carl Zeiss AG, Jena, Germany) The length, width, and thickness directions of the specimens were defined as the rolling direction (RD), transverse direction (TD), and normal direction (ND), respectively. The EBSD specimens were ground and polished first, and then mechanically polished until the surface was bright and there were no visible scratches under the optical microscope. Final electrolytic polishing was performed using the solution mixed with 10% perchloric acid and 90% alcohol. The electrolyte temperature, electrolytic voltage, and electrolytic time were −30 °C, 15 V, 120 s, respectively. The microstructure of the deformed samples was observed by transmission electron microscopy (TEM, JEM-2100 JEOL Tokyo, Japan). The parameters were as follows: LaB6 electron gun of spot resolution 0.23 nm, line resolution 0.14, and working voltage 200 kV. The preparation process of the TEM sample was as follows: 600 μm thick samples were cut along the direction perpendicular to the tensile axis 5 mm from the fracture. The sample was ground to 50 μm. A TJ100-SE (LEBO China) electrolytic double jet thinning instrument was used to prepare transmission samples. The solution was a mixture of alcohol and perchloric acid with a volume ratio of 9:1.

3. Results and Discussion

3.1. Phase Composition Analysis

In order to determine whether the phase composition of the welded joints changed with different coating amounts of activated flux, the phase composition of the welded joints was analyzed by XRD. During the test, XRD analysis was conducted on different areas of the welded joint, including the base metal, the weld seam and heat affect zone (HAZ), and the results are shown in Figure 1. The phase compositions of the weld seam hardly changed under different coating amounts of activated flux, all of which were composed of α-Mg, Al_2Mg, MgZn, and MgO [34]. Among them, α-Mg should be the matrix, Al_2Mg and MgZn should be the second phase, and MgO should be slag inclusions (formed due to poor protection during welding). With the increase in activated flux amounts, the diffraction peaks were not obviously broadened. Based on Scherrer Formula [35], it can be inferred that the lattice distortion is small.

$$D = K\lambda/\beta\cdot\cos\theta \tag{1}$$

where K is Scherrer constant, 0.89 or 1, D is grain size, λ is X-ray wavelength, β is peak width, θ is diffraction angle.

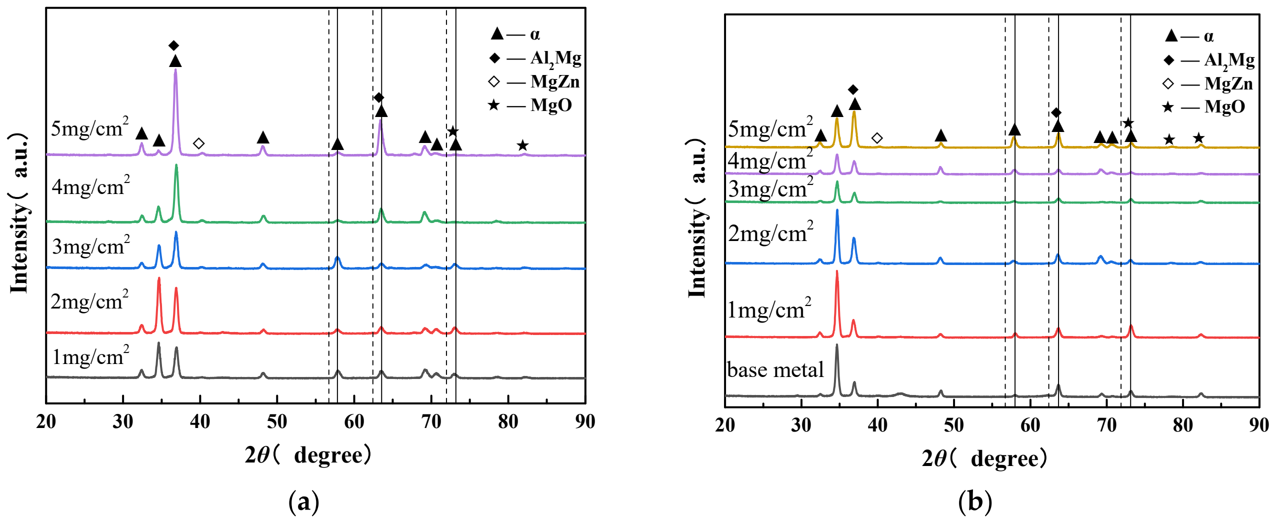

Figure 1. XRD results of welded joints. (**a**) Weld seam; (**b**) base metal and HAZ.

With the increase in activated flux amounts, the diffraction peaks of the weld seam still changed to some extent (see Figure 1a). Firstly, with the increase in activated flux amounts, the relative intensities of diffraction peaks changed. When the coating amount of activated flux is less than 2 mg/cm^2, the strongest diffraction peak was the (002) crystal plane of α-Mg, and as the coating amount of activated flux further increased, the strongest diffraction peak changed to (101) crystal plane of α- Mg. It showed that the microstructure of the weld seam had a certain orientation behavior, this will be specifically analyzed in the following section of EBSD. Secondly, as a second phase, the MgZn phase had a relatively weak diffraction peak when activated flux was relatively small, and the diffraction peak increased significantly with the increase in activated flux. It can be seen that the increase of activated flux was beneficial to the precipitation of MgZn. In addition, the diffraction peak of MgO also fluctuated to some extent under different coating amounts of activated flux. The relative intensity of the diffraction peak was very weak when the activated flux was 2 mg/cm^2 and 4 mg/cm^2. This indicated that the protective effect of shielding gas was better under the parameter and that the content of MgO in the weld seamwas less.

The five diffraction curves of the heat-affected zone shown in Figure 1b are consistent with the weld seam. However, the preferred crystal growth trend was not as obvious as the weld seam (except for the coating amount of activated flux at 5 mg/cm^2, the strongest diffraction peaks under other coating amounts are (002) crystal plane). This is mainly related to the physical and metallurgical process of welding. During the welding process, the HAZ was in the middle of the base metal and weld seam, which is a semi-melting state. Therefore, its microstructure, nucleation and phase composition retained more original information of the base metal. Furthermore, the diffraction results of the weld seam and HAZ had a common feature, that is, the overall diffraction peaks were shifted to the right by 0.39°. The phenomenon did not disappear after several adjustments to the test equipment and according to the Bragg equation, this was a typical manifestation of grain refinement.

3.2. Microstructure Analysis

Figure 2 shows the microstructures of the weld seam. There was little difference in microstructure and morphology in the weld seam under different amounts of activated flux.

The phase with dark gray is the α-Mg matrix, and the gray-white area is grain boundary. Certain amounts of second phases are distributed along the grain boundary, but the specific phase types cannot be directly concluded from the morphology. However, combined with the XRD results in Figure 1, it can be supposed that the grain boundary should contain Al_2Mg, MgZn, or other second phases.

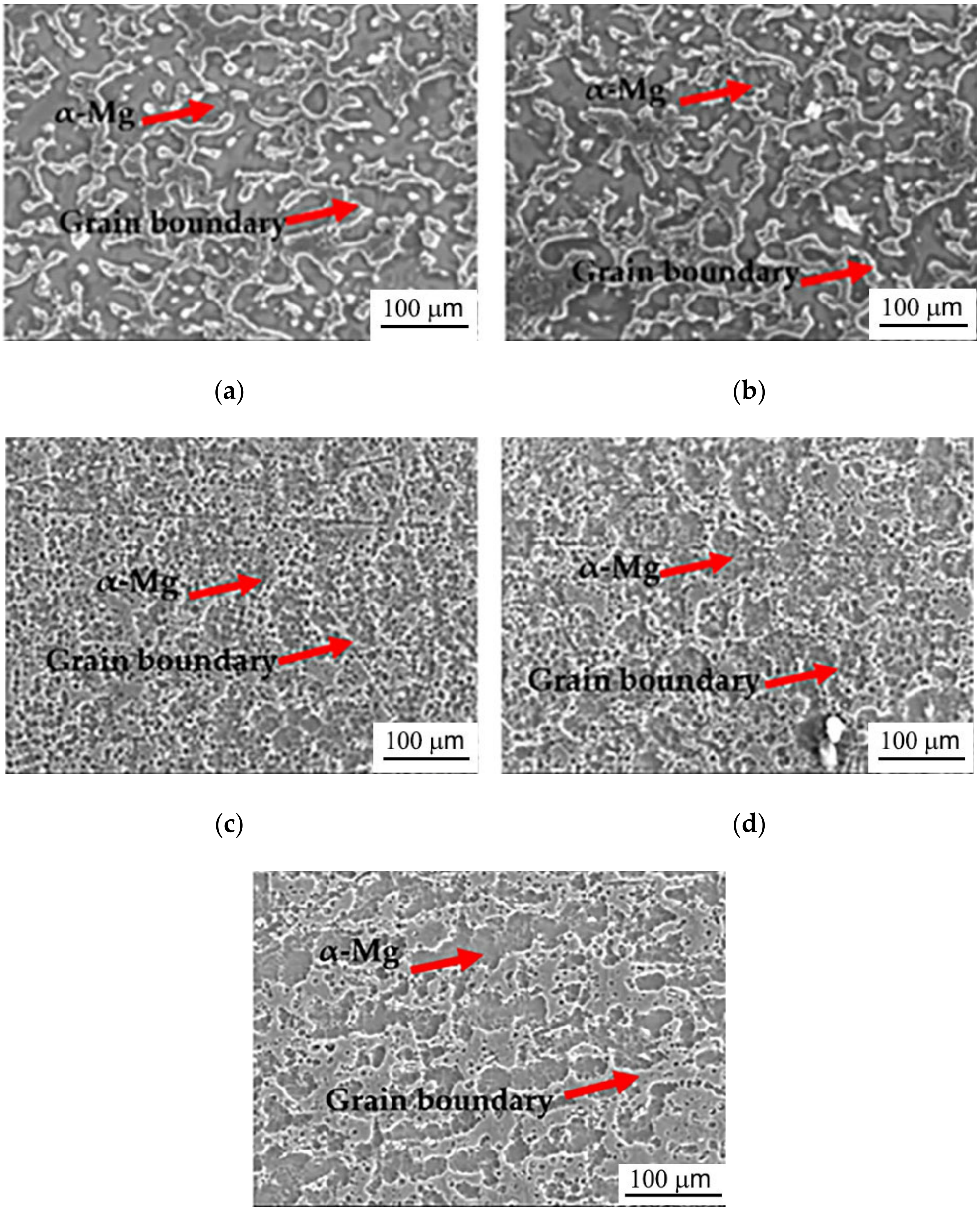

(**a**) (**b**) (**c**) (**d**) (**e**)

Figure 2. Microstructure of weld seam. (**a**) 1 mg/cm^2; (**b**) 2 mg/cm^2; (**c**) 3 mg/cm^2; (**d**) 4 mg/cm^2; (**e**) 5 mg/cm^2.

Although the morphology did not change, the grain size obviously changed. With the increase in activated flux amount, the grain size of the weld seam initially showed a tendency to be refined. The finest grains were obtained when the activated flux amount was 3 mg/cm^2 (as shown in Figure 2c). With a further increase of the activated flux amount, the grain size of the weld seam appeared to be a coarsening trend. The matrix phase α-Mg of the weld seam grew up significantly at the activated flux amount of 5 mg/cm^2. The above changes are detrimental to the mechanical properties of welded joints. This phenomenon is mainly caused by the combined action of the external magnetic field and activated flux. The external magnetic field can change the shape of the welding arc, driving it to rotate, forming a "bell jar" with a narrow top and a wide bottom. During the welding process, the chloride activated flux is ionized to form negative ions and adsorbs around the welding arc, which compresses the welding arc. Therefore, under the combined action of the external longitudinal magnetic field and chloride activated flux, the welding arc presented a compressed rotational motion mode. The rotation radius and speed of the welding arc improved to a certain extent under the appropriate parameters. The welding arc is the heat source carrier for welding. The moving arc will inevitably drives the molten pool to move accordingly, but the movement state of the molten pool is slightly behind the welding arc. Moreover, as a part of the entire circuit, the molten pool is both an electrical conductor and a magnetic path. Thus, the molten pool will also be driven to move by the electromagnetic force. Under the dual driving action, the molten pool motion speed of magnetron A-TIG welding is higher than that of traditional TIG welding. The high-speed movement of the molten pool changes the nucleation conditions and growth pattern of crystal, hence the mechanical properties of the weld seam are affected. On one hand, the moving pool generates a shear force on the columnar crystals that initially nucleates and grows attached to the base metal. When the shear force reaches a certain level, the columnar crystals are broken. The broken dendrite re-enters into the molten pool and becomes a heterogeneous nucleation source, which can inhibit the forming of columnar crystals and increase the nucleation rate. On the other hand, the moving molten pool promotes the temperature diffusion, thus reducing the temperature gradient and concentration fluctuations in the molten pool area and improving the formation of equiaxed crystals. Therefore, the finest grain of the weld seam was obtained when the coating amount of activated flux was 3 mg/cm^2. However, when the amount of activated flux increased further, the resistance heat generated was strengthened under the electromagnetic damping of external magnetic field and "insulation effect" of activated flux (the thermal conductivity of the $NiCl_2$ flux waslow, which causes heat to hardly spread in the weld seam, thus playing a heat preservation role). As a result, the overheating degree of the weld seam increased, which prolongs the high-temperature residence time of the molten pool and made the grain size of the weld seam coarse.

For further analysis, the welded joint at an activated flux amount of 3 mg/mm^2 was selected as the representative to compare the microstructure of different areas, including the base metal, HAZ, and the weld seam. The results are shown in Figure 3. It can be seen that the base metal is composed of equiaxed crystal and the grain boundary is clear. The morphology of the weld seam microstructure is obviously different from that of the base metal. The grain distribution is very messy and the grain boundaries are difficult to identify (as shown in Figure 3c). Because HAZ is located between the weld seam and the base metal, its microstructure retains some characteristics of the base metal. The grain boundary of HAZ is faintly visible, but its width is larger than that of the base metal, and the grain size increases. During the welding process, the base metal is rapidly heated to form a molten pool, and then is quickly cooled to form a welded joint. Due to the nucleation and growth of the weld seam under rapid cooling conditions, the morphology of the grain clearly deviates from the equilibrium state. This is why the microstructure morphology of the weld seam is different from the base metal. The HAZ is in a semi-solid state during the welding process, only a few crystals in HAZ have undergone phase transformation, so the characteristics of the base metal are largely preserved.

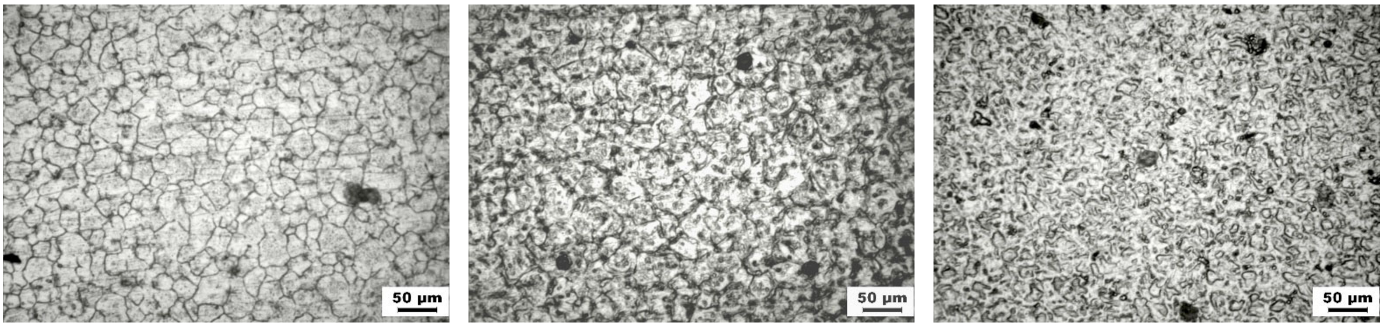

(a) (b) (c)

Figure 3. Microstructure of welded joint at activated flux amount of 3 mg/cm^2. (**a**) Base metal; (**b**) HAZ; (**c**) weld seam.

Due to the small size of the welding pool and the fast solidification speed, the metallurgical reaction process was relatively complex. The combined introduction of magnetic field and active agent further increased the complexity of the whole system. With the existing technical means, it was difficult to obtain the real movement pattern change of the molten pool by direct observation. Therefore, simulation software was used to study and analyze the movement pattern of the molten pool. The heat and mass transfer model of the molten pool is shown in Figure 4. Since the active agent cannot be added to the data model for the time being, only the motion state of the molten pool under different magnetic field conditions was analyzed. The model used Cartesian coordinate system to analyze the three-dimensional transient shape of the molten pool. The calculation and analysis process also followed the mass conservation equation, momentum conservation equation and energy conservation equation. The solution domain of simulation analysis was 80 mm × 60 mm × 5 mm, the grid was still divided with fine center and sparse edges, which ensures the calculation accuracy of the central area and considered the requirements of calculation time. The specific grid form, parameters and boundary conditions refer to previous research results [14]. The heat of the molten pool comes from the arc on the surface, and the heat conduction process includes the arc heat source input, heat conduction and radiation loss heat. The specific equation [36] was:

$$\kappa_{\mathrm{mg}} \frac{\partial T}{\partial z}\bigg|\mathrm{top} = \frac{3\eta\varphi I}{\pi{\sigma_j}^2} \exp\left(-\frac{3r^2}{{\sigma_j}^2}\right) - \sigma_b \varepsilon_{\mathrm{mg}}\left(T^4 - {T^4}_\infty\right) - h_c(T - T_\infty) \tag{2}$$

where κ_{mg} is the thermal conductivity of magnesium alloy, unit: w/MK; η is welding efficiency, φ is the welding arc potential, σ is the limited distribution radius of current, unit: mm; $\varepsilon_{\mathrm{mg}}$ is the emissivity of magnesium alloy surface, h_c is the heat transfer coefficient of magnesium alloy surface, unit: W/m^{2}k, and T_∞ is the ambient temperature.

In order to ensure consistency and the consistency of the data, the magnetic field parameters consistent with the arc shape were selected in the simulation process of the molten pool movement pattern, and the three-dimensional transient movement model of the molten pool was calculated according to the above theoretical model and control equation. The results are shown in Figure 5. There are three groups of pictures under different magnetic field intensities, which represent the surface (XY plane), cross section (XZ plane) and symmetry plane (YZ plane).

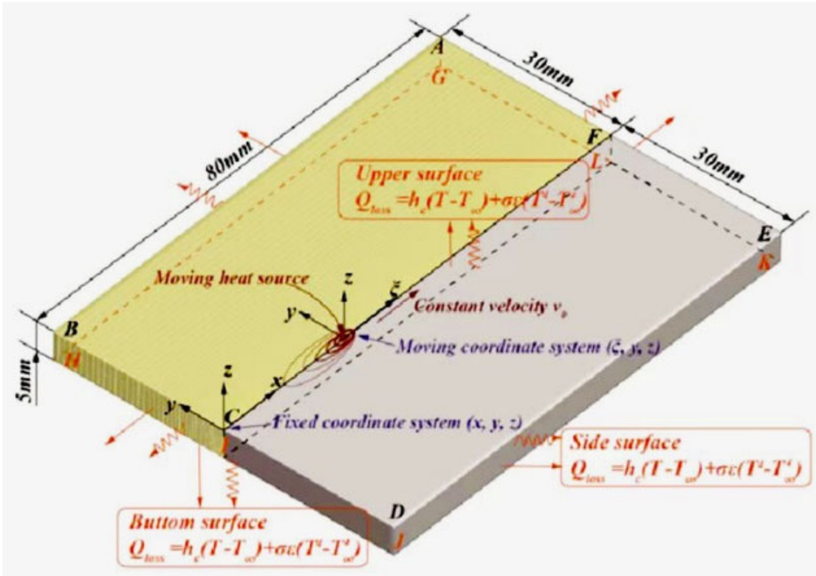

Figure 4. Heat and mass transfer model of molten pool.

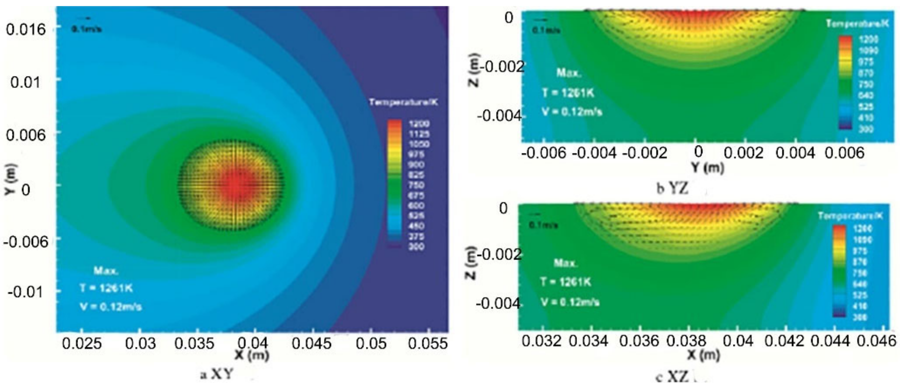

(**a**) B = 0 T

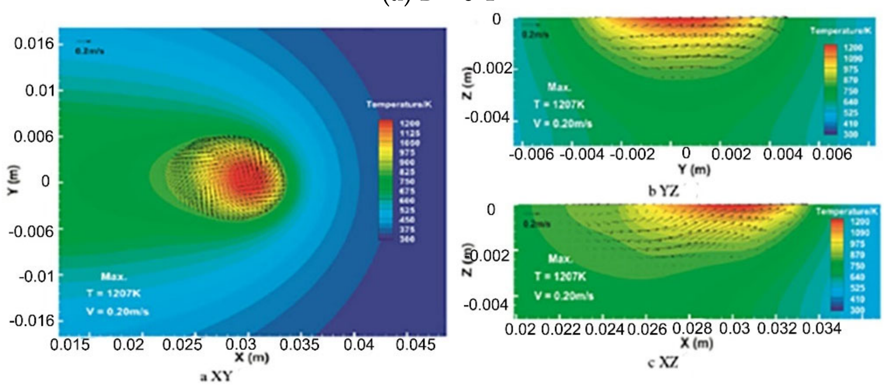

(**b**) B = 0.01 T

Figure 5. *Cont*.

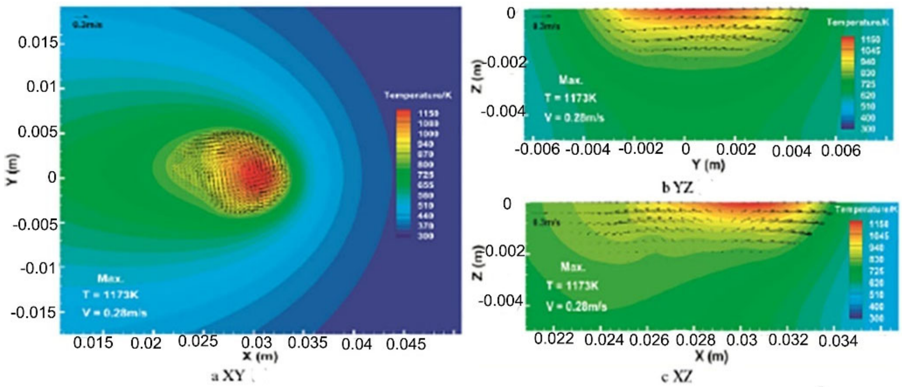

(**c**) B = 0.02 T

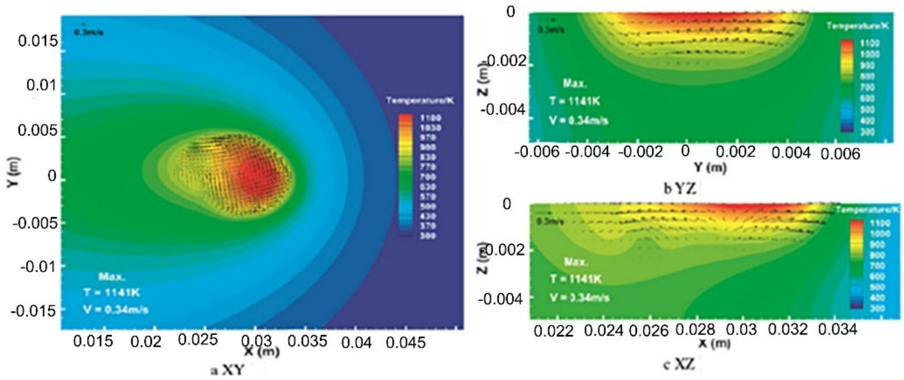

(**d**) B = 0.03 T

Figure 5. Temperature field and flow field of molten pool under different magnetic field strength.

Under the condition of no magnetic field, the molten pool was a typical TIG welding molten pool, with an overall axisymmetric shape. The liquid metal in the molten pool flowed from the central area to the surrounding area, with a maximum flow rate of 0.12 m/s and a maximum temperature of 1261 k, as shown in Figure 5a.

3.3. Change of Grain Size and Orientation of Weld Metal with and without Magnetic Field

With the introduction of the magnetic field, the motion shape of the molten pool changed, which was reflected in the following aspects: firstly, the original axisymmetric shape no longer existed, and the larger the magnetic field strength, the more obvious the distortion of the molten pool shape; secondly, the convection velocity of the molten pool tended to increase, while the maximum temperature tended to decrease (see Table 2 for specific data); thirdly, with the increase of the magnetic field strength, the internal eddy current at the tail of the molten pool was more obvious, forming the "trailing" phenomenon. This shows that the application of the magnetic field changed the movement shape of the molten pool and accelerated the movement of the molten pool. On the one hand, it makes the scouring effect on the crystal front of the molten pool more obvious, which is conducive to improving the nucleation rate of the molten pool metal and playing the role of refining the structure. On the other hand, the moving molten pool moves together with the pores and slag in the molten pool, accelerating the floating speed of these defects and also plays a positive role in purifying the structure. However, the appearance of "tailing" under a large magnetic field is unfavorable to welding. On the one hand, it increases the weld width and reduces the penetration depth, which reduces the welding efficiency. On the other hand, it is unfavorable to the weld formation, easily causing defects such as undercut, and affecting the use of products.

Table 2. Morphological data of molten pool under different magnetic field strength.

Number	Magnetic Field Intensity B/T	Maximum Temperature T/K	Maximum Flow Rate υ/m·s^{-1}	Movement Form
1	0	1261	0.12	The center moves freely around in an axisymmetric shape
2	0.01	1207	0.2	Directional rotary motion, non axisymmetric, with vortex at the tail
3	0.02	1173	0.28	Directional rotary motion, in non axisymmetric form, with vortex trailing behind
4	0.03	1141	0.34	Directional rotary motion, in non axisymmetric form, with vortex trailing behind

In order to verify and analyze the above simulation results, the actual forming state of the weld under different parameters was tested, and the results are shown in Figure 6. It can be seen from Figure 6 that the weld area is full and distributed axisymmetrically under the condition of no magnetic field, but the penetration depth is small and there is a certain surplus height. The application of the magnetic field made the weld forming state change to some extent. Although the weld zone basically presents an axisymmetric structure, the shape of the weld zone changed, the reinforcement height disappeared, and the penetration depth obviously increased, as shown in Figure 6b. However, when the magnetic field strength was large, the axisymmetric shape shifted, which indicates that the application of the magnetic field made the motion shape of the molten pool change significantly. This result is in good agreement with the simulation data, which indicated that the chloride mode is mainly arc and has limited influence on the motion shape of the molten pool, while the influence of the magnetic field on the molten pool was still dominant, as shown in Figure 6c.

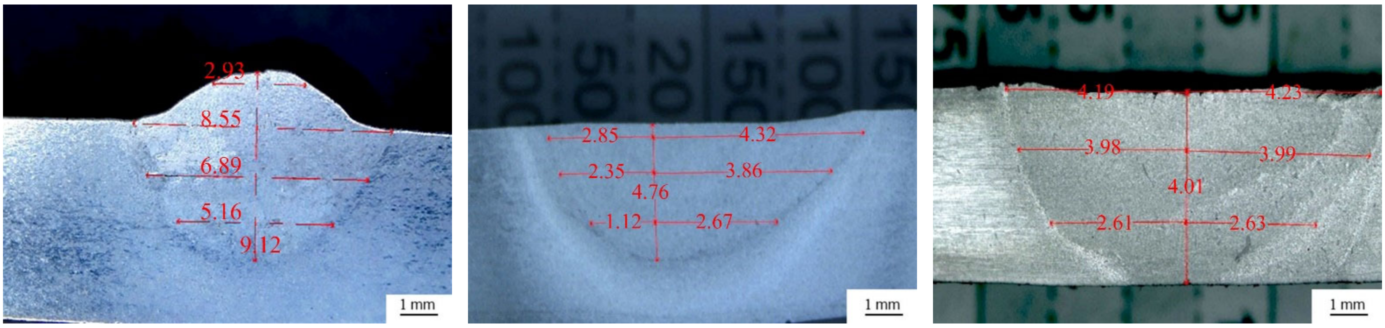

(**a**) (**b**) (**c**)

Figure 6. Physical map of weld formation under different technological conditions. (**a**) B = 0 T, (**b**) B = 0.03 T, (**c**) B = 0.03 T + 3 mg/cm^2 $NiCl_2$.

Metallographic analysis was only used to analyze the distribution morphology and size of grain. Aiming to reveal the law of crystal growth under the action of the magnetic field and activated flux, EBSD was used to analyze the crystal orientation behavior in the base metal and the weld seam under different activated flux amounts. The results are shown in Figures 7–9.

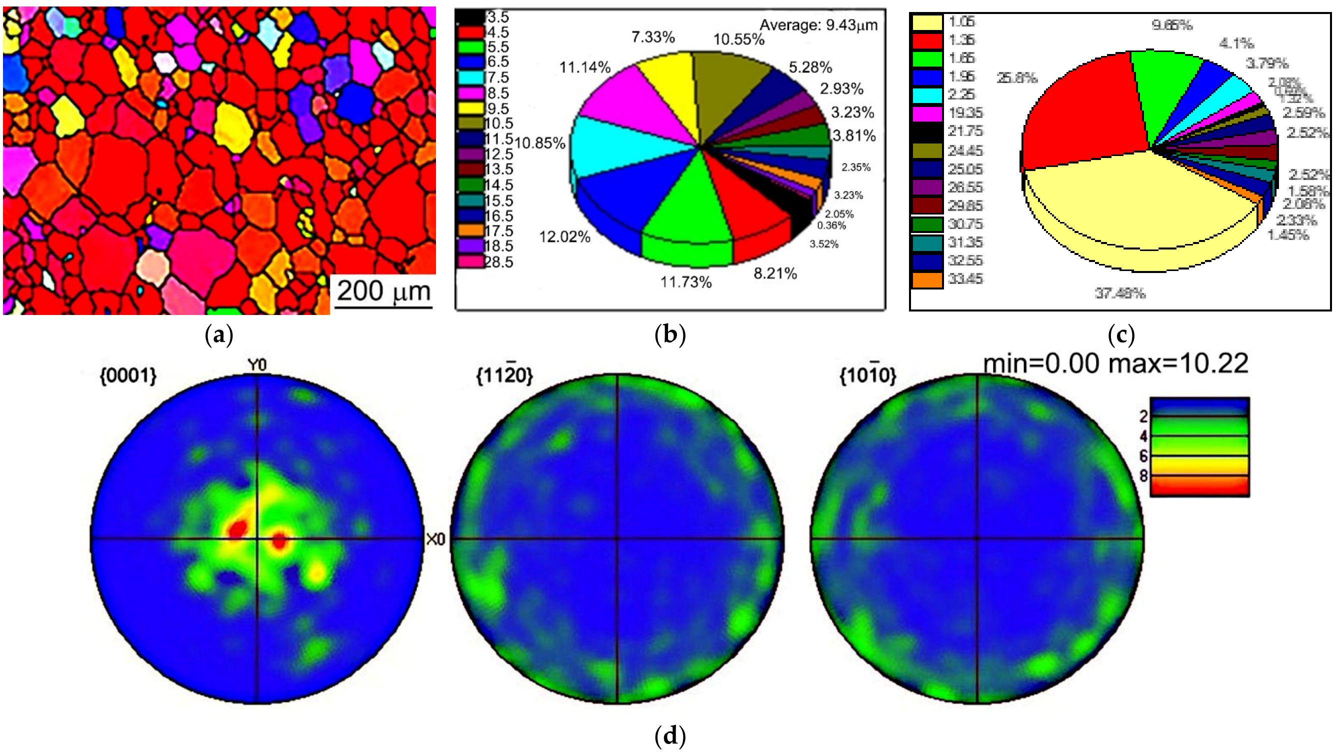

Figure 7. EBSD results of base metal. (**a**) Orientation image; (**b**) Grain size; (**c**) Misorientation angle; (**d**) Pole figure.

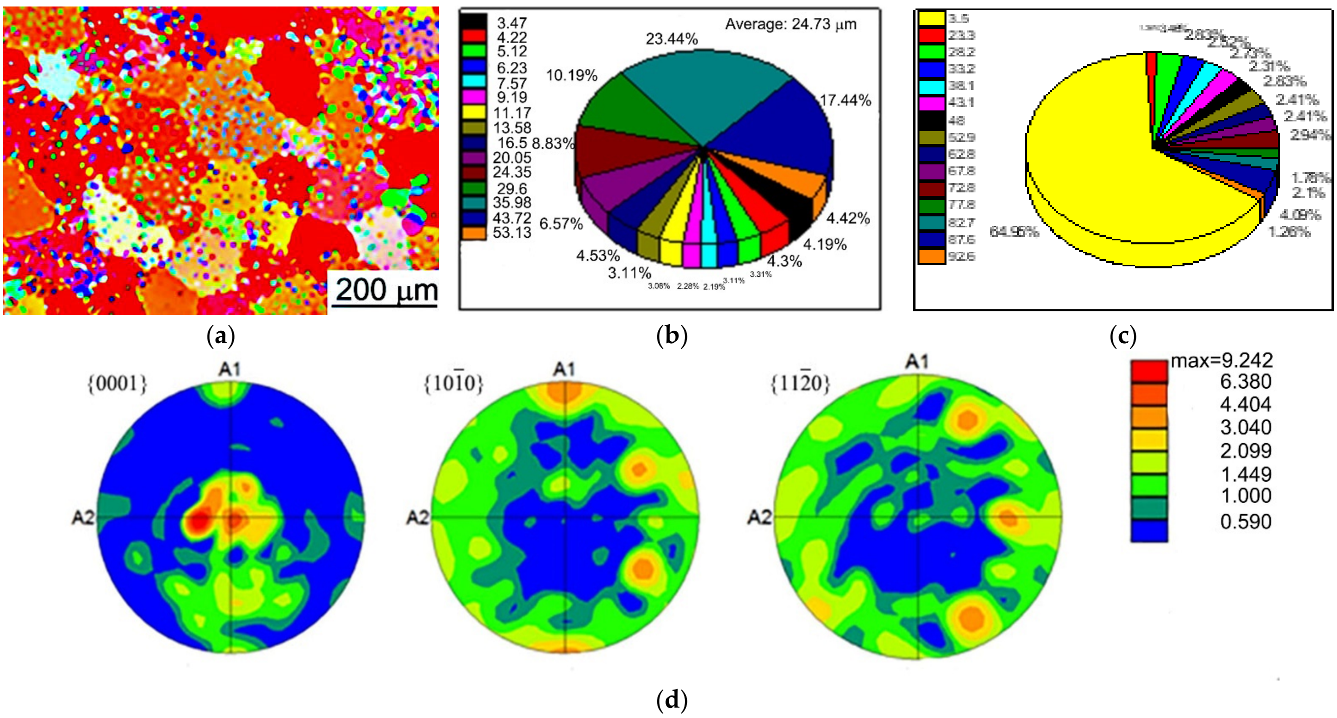

Figure 8. EBSD results of weld seam at flux coating amount of 1 mg/cm^2. (**a**) Orientation image; (**b**) arain size; (**c**) misorientation angle; (**d**) pole figure.

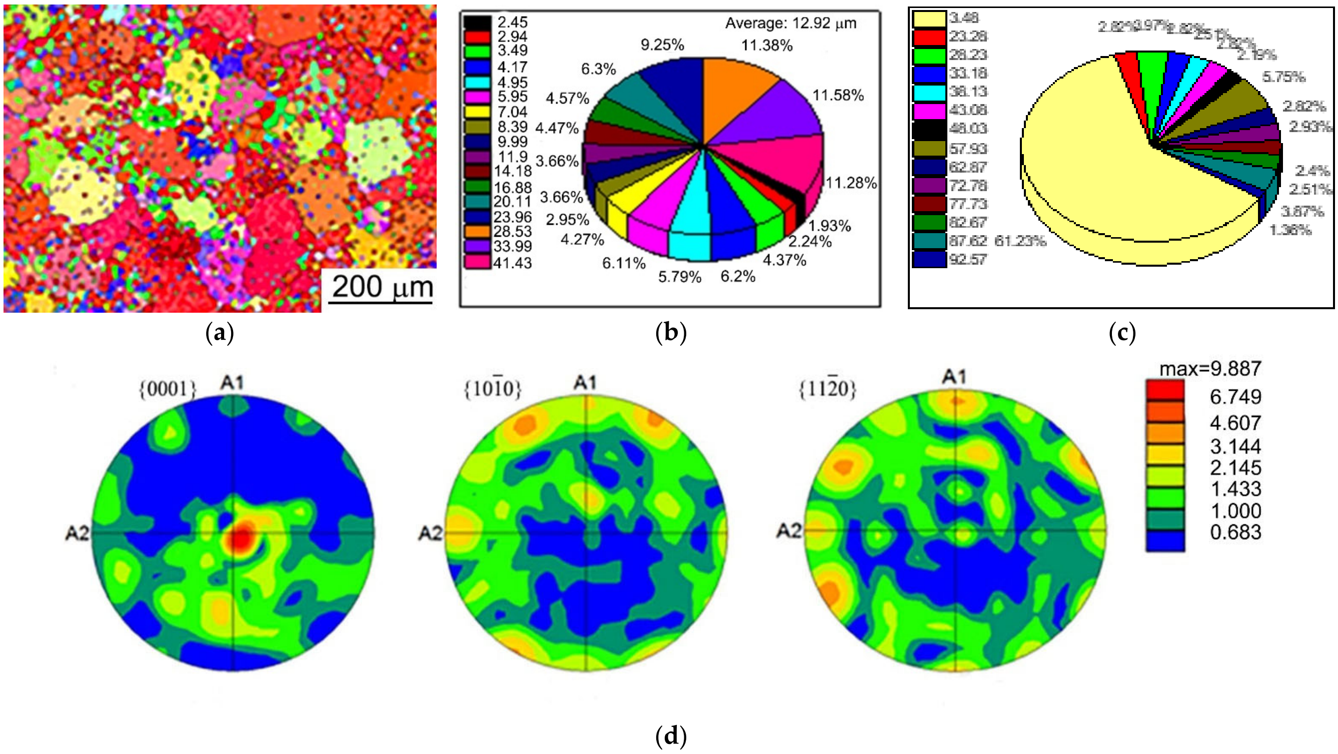

Figure 9. EBSD results of weld seam at flux coating amount of 3 mg/cm^2. (**a**) Orientation image; (**b**) grain size; (**c**) misorientation angle; (**d**) pole figure.

During the EBSD test, the backscatter diffraction peaks of different crystal planeswere calibrated, and different crystal plane orientation behaviors were characterized by different colors. The index of the crystal plane expressed in different colors refers to the bottom right corner of the reverse pole figure (see Figures 7a, 8a, and 9a). The microstructure orientation image of EBSD can be compared to the microstructure in Figures 2 and 3 for a better understanding of dendrite morphology. The supply state of AZ91 magnesium alloy used in the test was rolled state, the grains were intact and the grain boundaries were clear. When the external magnetic field was applied and the coating amount of activated flux was 1 mg/cm^2, the grain boundary was clear and the precipitates were relatively few. However, when the coating amount increased to 3 mg/cm^2, the precipitates at grain boundary significantly increased, the distribution of crystal plane was messy, and a large number of (100) and (110) crystal plane appeared. Through the statistics of grain size, it can be found that the average grain size of the base metal was 9.43 µm, the average grain size of the weld seam at the coating amount of 1 mg/cm^2 and 3 mg/cm^2 was 24.73 µm and 12.92 µm, respectively (see Figure 7b, Figure 8b, and Figure 9b). It can be seen that the combined effect of the magnetic field and activated flux on refining the grain size was very obvious, and the refining rate reached 47.8%. According to the Hall-Petch formula, it is beneficial to improve the comprehensive mechanical properties of the welded joint. However, the grain size of the weld seam was larger than that of the base metal. That is why the mechanical properties of the welded joint were lower than the base metal in fusion welding state.

The distribution densities of low-angle grain boundaries (LAGBs, with misorientation angles ranging from 2–15°) and high-angle grain boundaries (HAGBs, with misorientation angles higher than 15°) were quantified and are shown in Figures 7c, 8c, and 9c. When the coating amount of activated flux was 1 mg/cm^2, the LAGBs in the weld seam accounted for about 64.95%, and when the amount was 3 mg/cm^2, the LAGBs in the weld seam accounted for 61.23%. The misorientation angle distribution of the base metal was more dispersed than that of the weld seam, but it was still dominated by LAGBs. The misorientation angle of the base metal appeared at 1.05°, 1.35°, 1.65°, 1.95°, and 2.25°, the total proportion of LAGBs reached 80.83%, which was much higher than that of the weld seam under different amounts of activated flux. It was indicated that the grain boundaries in the weld seam under the two parameters were dominated by the LAGBs, but the proportion of LAGBs tended to decrease. The relationship between the low-angle grain boundary energy and the misorientation angle is shown as formula [37]:

$$\gamma = \gamma_0 \theta (A - ln\theta) \tag{3}$$

$$\gamma_0 = \frac{Gb}{4\pi(1-v)} \tag{4}$$

where γ is grain boundary energy, γ_0 is material coefficient, θ is misorientation angle, A is integration constant, G is trimming modulus, b is Burgers vector, v is Poisson's ratio.

According to the analysis result of EBSD, when the coating amount of activated flux was 1 mg/cm^2 and 3 mg/cm^2, crystallographic characteristics of grain boundaries both were LAGBs, the misorientation angle of LAGBs was 3.5° and 3.48°, respectively. Although the crystallographic characteristics of the base metal were mainly composed of LAGBs, the misorientation angle was relatively dispersed. It can be concluded that the change of activated flux coating amount does not affect the misorientation angle. According to formula (3), it can be obtained that for LAGBs, the interface energy increased with the increase of the misorientation angle. The introduction of activated flux can increase the interfacial energy. The higher the interfacial energy, the more unstable the grain boundary is and the greater the atomic mobility is [38]. Thus, the microstructure of the weld seam was obviously messier than the base metal.

The pole figure represents the position of a crystal with a certain orientation on a particular crystal plane {h k l}. Due to large amounts of information reflecting in the pole figure, it becomes an important link in the analysis of EBSD data. If there is no texture in a polycrystalline material, the polar map density will be randomly distributed throughout the sphere. The poles are evenly distributed on the pole figure. Otherwise, the distribution will be uneven [39]. The distribution of crystal poles in the weld seam was obviously uneven (see Figures 8d and 9d). In the pole figure, the (0001) crystal plane shows obvious highlighted areas, indicating that the crystal had a tendency of preferential growth on the (0001) crystal plane. When the activated flux was 1 mg/cm^2, there are two high-density regions in (0001) crystal plane of the pole figure, which was similar to the base metal. It indicated that when the coating amount of activated flux is small, the grain growth pattern of the weld seam still retains the basic characteristics of the base metal. However, when the coating amount was 3 mg/cm^2, the (0001) crystal plane in the pole figure only had a high-density zone at the pole. The result displays that the increase of the flux coating amount changes the preferential growth behavior of crystals. In addition, the welding arc is plasma, which has good conductivity, electrical quasi-neutrality, and interaction with magnetic field. Under the external alternating longitudinal magnetic field, the welding arc rotated. Under the action of the alternating magnetic field, the liquid metal in the molten pool produced an induced current, and the electromagnetic interaction between the magnetic field and the induced current produced Lorentz force. The rotating welding arc and the electromagnetic force generated by the interaction between the external magnetic field and the current in the molten pool produce a strong electromagnetic stirring effect on the liquid metal in the molten pool, which made the liquid metal in the molten pool flow rapidly and generate forced convection. The stirring effect of the external magnetic field on the liquid metal in the molten pool made it difficult for the dendrites to grow up, or they were broken or broken during the solidification process. These broken dendrites left the side wall of the molten pool and entered the molten pool. They became new growth centers when they were free in the liquid at the crystallization front. Convection rought grains separated from the side wall of the molten pool and nucleating particles separated from the molten pool to the composition supercooling zone at the front of the solid-liquid interface, promoting heterogeneous nucleation, which greatly increased the nucleation rate of the melt and refined the weld microstructure.

Slip and twin are the two main deformation modes of materials. The crystal structure of AZ91 magnesium alloy is a hexagonal close-packed (HCP) structure, the slip systems of AZ91 magnesium alloy is only three. Therefore, the plastic deformation of magnesium alloy is difficult to be realized by crystal slip, but mainly depends on twin. The twins can be found in the EBSD diagram, of which red regions are (10–12) twins after analysis, seen in Figures 7a, 8a, and 9a. In order to reflect the distribution of twins more clearly, the weld seam was analyzed by TEM when the activated flux was 3 mg/cm^2. The result is shown in Figure 10. Twins and twin boundaries were clearly observed, and high-density dislocations accumulated in the twin boundary. The formation of these twins was caused by shear stress. At the same time, it was also the result of dislocation motion. The increase in these twins had a positive effect on the mechanical properties of the weld seam. On the one hand, the twin can release stress, reduce crack nucleation, passivate the crack tip, and hinder crack growth. Thus, the appearance of twins had a positive effect on preventing heat crack of magnesium alloy. On the other hand, the increase in twins will inevitably increase the number of twin boundaries. The twin boundary can separate the original grain, refine the grain and enhance the effect of fine grain strengthening. Moreover, the increase of twins can also adjust the grain orientation, which makes more slip system be in the soft orientation, and then activate the slip system, thus improving the toughness [40,41].

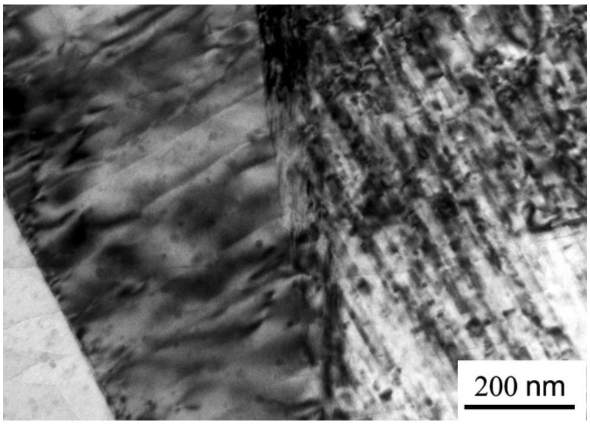

Figure 10. TEM of weld seam with 3 mg/cm^2 activated flux and magnetic field.

4. Conclusions

In this paper, AZ91 magnesium alloy was welded by TIG welding with activated flux and external longitudinal alternating magnetic field. The phase composition and microstructure evolution were investigated. The practical results were follows:

1. The phase composition of the welded joint was not changed under the introduction of magnetic field and activated flux, no new phase was formed. However, the growth patterns of grain in the weld seam and HAZ were different.
2. Under the combined action of the magnetic field and activated flux, the grain size of the weld seam was refined. When the coating amount of activated flux was 3 mg/cm^2, the finest grain in the weld seam was obtained, which was 12.92 μm. However, the grain size of the weld seam was larger than the base metal.
3. The crystallographic characteristics of grain boundaries in the weld seam and base metal both were LAGBs. The misorientation angle and interfacial energy increased with the increase of the coating amount of activated flux. Therefore, more unstable grain boundaries were obtained. The microstructure of the weld seam was messier than the base metal.
4. Under the combined action of magnetic field and activated flux, the crystallization nucleation condition of the molten pool was changed, which promoted the formation of twins and made the crystal selectively grow parallel with the (0001) basal plane.

Author Contributions: G.Z. conceived and designed the experiments; Y.R. performed the experiments and collected the data; Y.S. analyzed the data and drafted the paper. All authors have read and agreed to the published version of the manuscript.

Funding: The authors acknowledged the financial support by National Key Research and Development Plan of China (2017YFB1103603), Liaoning Key Laboratories, Shenyang University of Technology (20162408).

Data Availability Statement: The data that supports the findings of the study is available from the corresponding author, G.Z. and Y.S., upon reasonable request.

Conflicts of Interest: The authors declare no conflict of interest.

References

1. Wendt, A.; Weiss, K.; Ben-Dov, A.; Bamberger, M.; Bronfin, B. Magnesium Castings in Aeronautics Applications Special Requirements. In *Essential Reading in Magnesium Technology*; Springer: Cham, Switzerland, 2016; Volume 7, pp. 65–69.
2. Muttana, S.B.; Aggarwal, D. Prospects of magnesium for automotive lightweighting applications—part II. *Auto. Tech. Reviw* **2015**, *4*, 18–23. [CrossRef]
3. Ramalingam, V.V.; Ramasamy, P.; Kovukkal, M.D.; Myilsamy, G. Research and development in magnesium alloys for industrial and biomedical applications: A review. *Met. Mater. Int.* **2020**, *26*, 409–430. [CrossRef]
4. Li, Y.; Cheng, P.Y.; Hua, L. Current application of magnesium alloy in automotive industry and 3C product fields. *Jiangxi Nonf. Met.* **2007**, *21*, 30–33.
5. Lu, C.F.; Li, Y.J.; Zhang, K.; Li, X.G.; Ma, M.L.; Shi, G.L.; Yuan, J.W. Effect of welding current on microstructure and properties of TIG welded EW75 magnesium alloy. *Mater. Sci. Forum.* **2016**, *3960*, 142–148. [CrossRef]
6. Yang, S.Y.; Zhang, B.L. Experimental study of electron beam welding of magnesium alloys Electron beam welding properties of pure magnesium and AZ31 magnesium alloys. *Rare Met.* **2011**, *30*, 364–369. [CrossRef]
7. Asahina, T.; Tokisue, H. Electron beam weldability of pure magnesium and AZ31 magnesium alloy. *Mater. Trans.* **2001**, *42*, 2345–2353. [CrossRef]
8. Zhang, X.B.; Zhan, Y.C. Pulsed Nd: YAG laser spot welding of an AZ31 magnesium alloy. *Int. J. Adv. Manuf. Technol.* **2019**, *104*, 3053–3063. [CrossRef]
9. Shahnam, A.; Karimzadeh, F.; Golozar, M.A.; Hosseini, S.N. Microstructure evolution of ultra-fine- grained AZ31B magnesium alloy produced by submerged friction stir processing. *J. Mater. Eng. Perform.* **2019**, *28*, 4593–4601. [CrossRef]
10. Mironov, S.; Sato, Y.S.; Kokawa, H. Influence of welding temperature on material flow during friction stir welding of AZ31 magnesium alloy. *Metall. Mater. Trans. A* **2019**, *50*, 2798–2806. [CrossRef]
11. Hu, Y.B.; Zhao, C.; Deng, J. Research status and prospects of magnesium alloys welding technology. *Hot Work. Technol.* **2010**, *39*, 124–128.
12. Maduraimuthu, V.; Vasudevan, M.; Parameswaran, P. Studies on improvement of toughness in modified 9Cr-1Mo steel A-TIG weld joint. *Trans. Indian Inst. Met.* **2015**, *68*, 181–189. [CrossRef]
13. Gao, X.G.; Dong, J.H.; Han, X. Effect of RE2O3 (RE = La, Ce) fluxes on A-TIG welding of Ti6Al4V. *Int. Adv. Manuf. Technol.* **2017**, *91*, 1181–1188. [CrossRef]
14. Liu, H.L.; Wu, T.M. Effects of activating flux on weld bead geometry of inconel 718 alloy TIG welds. *Mater. Manuf. Process.* **2012**, *27*, 1457–1461.
15. Maduraimuthu, V.; Vasudevan, M.; Muthupandi, V.; Bhaduri, A.K.; Jayakumar, T. Effect of activated flux on the microstructure, mechanical properties, and residual stressed of modified 9Cr-1Mo steel weld joints. *Metall. Mater. Trans. B* **2012**, *43*, 123–132. [CrossRef]
16. Mary, M. Theoretical and experimental assessment of chloride effects in the A-TIG welding of magnesium. *Weld. World* **2002**, *46*, 7–21. [CrossRef]
17. Liu, L.M.; Zhang, Z.D.; Song, G.; Wang, L. Mechanisum and microstructure of oxide fluxes for gas tungsten arc welding of magnesium alloy. *Metall. Mat. Trans. A* **2007**, *38*, 649–658. [CrossRef]
18. Zhang, Z.D.; Liu, L.M.; Sun, H.; Wang, L. AC TIG welding with single-component oxide activating flux for AZ31B magnesium alloys. *J. Master. Sci.* **2008**, *43*, 1382–1388. [CrossRef]
19. Huang, Y.; Fan, D.; Lin, T.; Shao, F. Effects of activating fluxes on DCSP A-TIG weld penetration of magnesium alloy. *Trans. China Weld. Inst.* **2007**, *28*, 21–24.
20. Shen, J.; Wang, L.Z.; Peng, D.; Wang, D. Effects of CaF2 coating on the microstructures and mechanical properties of tungsten inert gas welded AZ31 magnesium alloy joints. *Metall. Mat. Trans. A* **2012**, *43*, 4397–4405. [CrossRef]
21. Liu, Z.J.; Lu, L.; Su, Y.H. Weld penetration increasing mechanism of magnesium alloy with oxide activating fluxes. *J. Shenyang Univ. Technol.* **2015**, *37*, 138–147.
22. Qin, B.; Yin, F.C.; Zeng, C.Z.; Xie, J.C.; Shen, J. Microstructure and mechanical proerties of TIG/A-TIG welded AZ61/ZK60 magnesium alloy joints. *Trans. Nonferrous Met. Soc.* **2019**, *29*, 1864–1872. [CrossRef]

23. Shen, J.; Zhai, D.J.; Liu, K.; Cao, Z.M. Effects of welding current on properties of A-TIG welded AZ31 magnesium alloy joints with TiO2 coating. *Trans. Nonferrous Met. Soc. China* **2014**, *24*, 2507–2515. [CrossRef]
24. Li, S.Z. Effects of the Welding Parameters and Hot Treatment on the Microstructures and Mechanical Properties of Tungsten Inert Gas Welded AZ31B Magnesium Alloy Joints. Master's Thesis, Chongqing University Chongqing, Chongqing, China, 2013.
25. Zhou, M.B.; Shen, J.; Hu, D.; Gao, R.H.; Li, S.Z. Effects of heat treatment on the activated flux TIG-welded AZ31 magnesium alloy joints. *Int. J. Adv. Manuf. Technol.* **2017**, *92*, 3983–3990. [CrossRef]
26. Shen, J.; Liu, K.; Li, Y.; Li, S.Z.; Wen, L.B. Particles and microstructures and mechanical properties of nanoparticles strengthening A-TIG(NSA-TIG) welded magnesium alloy joints. *Sci. Technol. Weld. Join.* **2013**, *18*, 404–413. [CrossRef]
27. Liu, X.G.; Guan, Z.Q.; Zhang, H.X.; Chang, Y.L. Research status and future prospects of magnesium control TIG welding technology. *Hot Work. Technol.* **2019**, *48*, 1–5.
28. Huang, M.Q.; Zhou, Q.; Liu, F.; Huang, J.J. Effect of DC magnetic field on solidifield structure and mechanical properties of AZ91D magnesium alloy. *Spec. Cast. Nonferr. Alloy* **2016**, *36*, 320–323.
29. Demchenko, V.L.; Yurhenko, M.V. Structure and properties of the welded joints of single-type polyethylenes formed under the action of constant magnetic fields. *Mater. Sci.* **2017**, *53*, 186–193. [CrossRef]
30. Hu, S.P.; Chen, L.P.; Zhou, Q.; Wang, J.; Zhang, L.; Wu, H. Effects of compound magnetic field of pulsed and alternate field on solidified structure and mechanical properties of AZ31 magnesium alloy. *Spec. Cast. Nonferr. Alloy* **2018**, *38*, 303–308.
31. Su, Y.H.; Jiang, H.W.; Wu, D.; Liu, Z.J. Optimum design of magnesium alloy welding parameters with GTAW under magnetic field. *Trans. China Weld. Inst.* **2012**, *33*, 85–88.
32. Su, Y.H.; Jiang, H.W.; Qin, H.; Liu, Z.J. Forming characteristics, microstructure and properties of magnesium alloy during TIG welding under magnetic field. *Trans. China Weld. Inst.* **2013**, *34*, 85–88.
33. Su, Y.H.; Liu, Z.J.; Liu, D. Effect of magnetic field frequency on microstructure and properties of AZ31 magnesium alloy welded joint with GTAW. *Adv. Mater. Res.* **2011**, *1335*, 882–885. [CrossRef]
34. Zhang, G.Q.; Ren, Y.L.; Su, Y.H. Research for microstructure and mechanical properties of AZ91 magnesium alloy welded joint with magnetic field and activated flux. *Mater. Res. Express* **2020**, *7*, 056511.
35. Patterson, A. The Scherrer Formula for X-Ray Particle Size Determination. *Phys. Rev.* **1939**, *56*, 978–982. [CrossRef]
36. Li, S.B.; Yang, J.T.; Du, W.B. A review on thermal conductivity of magnesium and its alloys. *J. Magnes. Alloy.* **2020**, *8*, 78–90. [CrossRef]
37. Wang, X.W.; Wang, C.J.; Liu, Y. An energy based modeling for the acoustic softening effect on the Hall-Petch behavior of pure titanium in ultrasonic vibration assisted micro-tension. *Int. J. Plast.* **2020**, *136*, 102879. [CrossRef]
38. Hu, G.Y.; Cai, X.; Rong, Y.H. *Fundamentals of Materials Science*; Shanghai Jiaotong University Press: Shanghai, China, 2010.
39. Mao, W.P.; Yang, P.; Chen, L. *Material Texture Analysis Principle and Detection Technology*; Metallurgical Industry Press: Beijing, China, 2008.
40. Zhang, X.Y.; Tu, J.; Liu, Q. High-resolution electron microscopy study of the {10-11} twin boundary and twinning dislocation analysis in deformed polycrystalline cobalt. *Scr. Mater.* **2012**, *67*, 991–994. [CrossRef]
41. Zhang, X.Y.; Zhu, Y.T.; Liu, Q. Deformation twinning in polycrystalline Co during room temperature dynamic plastic deformation. *Scr. Mater.* **2010**, *63*, 387–390. [CrossRef]